Nanodroplet Depinning from Nanoparticles

Qi Liu,[†,‡,§,∥,¶] Fong Yew Leong,[⊥,¶] Zainul Aabdin,[†,‡,§,∥] Utkarsh Anand,[†,‡,§,∥] Tran Si Bui Quang,[⊥] and Utkur Mirsaidov*[,†,‡,§,∥]

[†]Department of Physics, National University of Singapore, 2 Science Drive 3, Singapore 117551, [‡]Centre for Advanced 2D Materials and Graphene Research Centre, National University of Singapore, 6 Science Drive 2, Singapore 117546, [§]Centre for BioImaging Sciences, Department of Biological Sciences, National University of Singapore, Science Drive 4, Singapore 117543, [∥]Nanocore, National University of Singapore, 4 Engineering Drive 3, Singapore 117576,, and [⊥]A*STAR Institute of High Performance Computing, 1 Fusionopolis Way, Connexis, Singapore 138632. [¶]Q.L. and F.Y.L. contributed equally.

ABSTRACT Nanoscale defects on a substrate affect the sliding motion of water droplets. Using *in situ* transmission electron microscopy imaging, we visualized the depinning dynamics of water nanodroplets from gold nanoparticles on a flat SiN_x surface. Our observations showed that nanoscale pinning effects of the gold nanoparticle oppose the lateral forces, resulting in stretching, even breakup, of the water nanodroplet. Using continuum long wave theory, we modeled the dynamics of a nanodroplet depinning from a nanoparticle of comparable length scales, and the model results are consistent with experimental findings and show formation of a capillary bridge prior to nanodroplet depinning. Our findings have important implications on surface cleaning at the nanoscale.

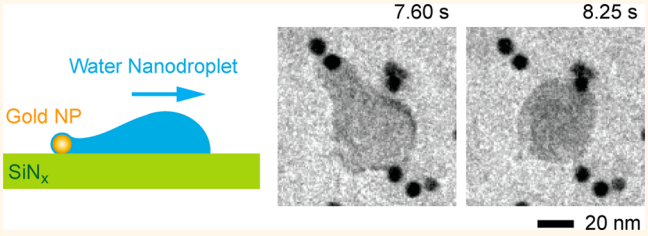

KEYWORDS: interfacial water · interfacial liquid · three-phase contact line · nanodroplet · *in situ* TEM · droplet pinning

Wetting and dewetting of solid surfaces[1] is dominated by pinning and depinning dynamics of the three-phase contact line on defect sites.[2] These defect sites can be a few nanometers in size, which makes visualizing their effect on the contact line experimentally challenging.[3] The pinning of a droplet on a rough surface alludes to interesting phenomena such as the coffee-ring effect,[4] leading to evaporative self-pinning[5] and fractal-like deposition patterns.[6] In addition, unusual wetting and spreading behavior[7] has been observed on surfaces decorated with nanoscale topographical features.[8] Nanotextured surfaces are currently being exploited for their superhydrophobic properties[9] and related applications including drag reduction,[10,11] self-cleaning,[12,13] and anti-biofilm formation.[14,15] Fine control of minute quantities of fluid on surfaces is of substantive interest in nanofluidic applications,[16,17] including nucleation of water droplets,[18] heat of condensation and transfer,[19] and surface mobility for water collection.[20]

The practical problem of whether a droplet slides or sticks on a surface depends largely on the underlying interfacial pinning forces.[21] If a droplet is much larger than the nanoparticles on the surface, the droplet could be treated as if it were pinned on a heterogeneous surface.[22,23] In contrast, if the drop and the particle are both comparable in size, then the solid particle presents an obstacle which directly imposes on the drop behavior.[24] However, it is not clear if the nanoscale depinning would be similar to that of bulk. Specifically, we question if a capillary bridge forms during pinch-off and if a threshold force is necessary to depin the nanoscale droplet completely from the nanoparticle. Due to recent advances in *in situ* electron microscopy,[25,26] it is now possible to probe the nanoscale dynamics of fluids experimentally. Previous studies on nucleation[27,28] of nanodroplets and nanobubbles,[29,30] migration of nanodroplets,[31,32] and confined liquids[33,34] using this approach revealed that, while electron beam effects drive these processes, the general properties of fluids appear to be unaffected. Therefore, *in situ* transmission electron microscopy (TEM) is ideally suited for exploring how the classical description of fluid behavior extends into the nanoscale.

* Address correspondence to phyumm@nus.edu.sg.

Received for review May 21, 2015 and accepted August 18, 2015.

Published online August 18, 2015
10.1021/acsnano.5b03078

In this study, we report our direct experimental observations of water nanodroplets in close proximity to gold nanoparticles, which act as pinning sites on an otherwise flat substrate. Using numerical modeling, we further investigate the morphology and dynamics of a nanodroplet under lateral force. We describe the forces necessary for depinning from the nanoparticles, which is on the order of nanonewtons, and compare the results against our experimental observations.

RESULTS AND DISCUSSION

Our experiments were performed with a FEI Tecnai TEM with an electron accelerating voltage of 120 kV and an electron flux range of 100−300 $e/(Å^2 \cdot s)$ and imaged at 20−25 frames per second using a CCD camera.[31] Briefly, we employed an environmental liquid cell to protect our water sample from the vacuum of the TEM column.[25,26] The liquid cells were microfabricated from silicon, which had a ∼20 nm thick electron translucent silicon nitride (SiN_x) membrane window with lateral dimensions of $\sim 20 \times 50\,\mu$m. The root mean square roughness of the membrane was ∼0.2 nm with a peak-to-peak value of ∼1 nm (Supporting Information Figure S1). An approximately 100 nm gap was formed between the membranes controlled by the spacer (Figure 1A). Water containing 10 or 20 nm gold nanoparticles in pure water was loaded into the liquid cell to fill this gap between the two membrane windows. The water with nanoparticles was sealed into the chip with a copper gasket and vacuum grease.

During TEM operation, the electron beam passes through the top and the bottom membrane windows and the enclosed film of water. As we expose the water to the electron beam irradiation, the thick water film (∼100 nm) retracts from the illuminated area of the membrane window, leaving behind a thin water film (∼10−20 nm). As the thin film dewets, residual nanodroplets that are 20−80 nm in diameter remain on the SiN_x surface coated with gold nanoparticles. When illuminated by an electron beam, the nanodroplets can be induced to move by the very same electron beam used for imaging (Figure 1B,C),[31] where these nanodroplets translocate through a series of stick−slip steps, as shown in the case of a 30 nm diameter nanodroplet moving across the 10 nm gold nanoparticles in Figure 1C−E.

The motion of water nanodroplets on the membrane surface scattered with 20 nm gold nanoparticles is shown in Figure 2 (Supporting Information video 1). Once the nanodroplet comes into contact with the nanoparticle, it engulfs the particle and becomes pinned. While the nanodroplet remains pinned, its subsequent movements are restricted to the vicinity of this pinning site with its edge in constant contact with the nanoparticle (Figure 2C; t = 5.35−16.75 s). Only when the nanodroplet eventually depins from the nanoparticle does it continues its original movement

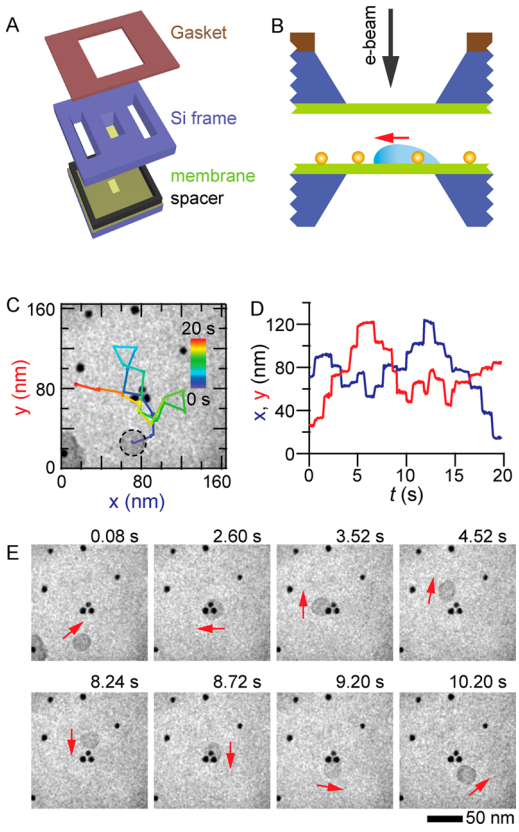

Figure 1. Experimental setup. (A) Schematic of the liquid cell and (B) experimental setup showing nanodroplet and gold nanoparticles on top of the membrane. (C) Trajectory of the ∼30 nm nanodroplet, and (D) corresponding coordinates of its center of mass. (E) Time series images showing nanodroplets at different stick position on a gold nanoparticle-coated SiN_x surface with stick−slip steps. Red arrows indicate the direction toward which the nanodroplet will move next.

on the membrane surface through the usual series of stick−slip steps (Figure 2C; t > 16.75 s).

Pinning of the nanodroplet to defect sites suggests that there is some degree of adhesion between water and gold molecules, consistent with the hydrophilic nature of gold.[35] Therefore, one expects that a minute trace of water would be left behind on the gold nanoparticle pinning sites, once the nanodroplet detaches from it. Figure 3 shows such a case where a nanodroplet that spreads as it moves forward forms a thin capillary bridge between the nanodroplet and the nanoparticle prior to depinning. Once the nanodroplet depins, it leaves behind a water film pinned on the nanoparticle, which then condenses into a smaller droplet, while a larger detached nanodroplet continues on its way. A small residual nanodroplet can also be retained by the nanoparticles due to the collapse of a capillary bridge, as discussed later.

To elucidate the physics of nanoscale depinning, we conducted numerical simulations based on an observed nanodroplet depinning from two closely spaced 10 nm particles but in different directions (Figure 4) (Supporting Information video 2). The physical model consists

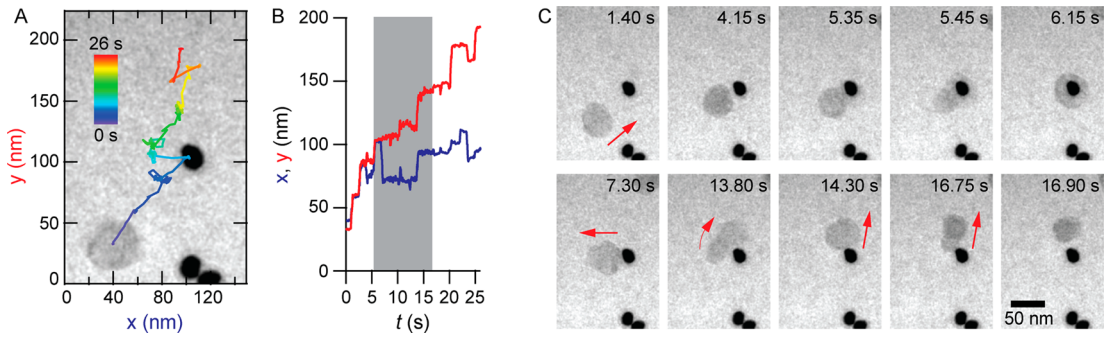

Figure 2. Pinning of the nanodroplet by a 20 nm nanoparticle. (A) $x-y$ coordinates of the nanodroplet on the SiN_x surface with 20 nm gold nanoparticles. (B) Coordinates of the nanodroplet's center of mass as a function of time. Here, the gray shaded regions indicate that the nanodroplet is in contact with 20 nm nanoparticle. Change in $x-y$ coordinates in the shaded region is due to rotation of the pinned nanodroplet around the nanoparticle. (C) Nanodroplet approaches the nanoparticle and engulfs it (top). Nanodroplet moves around the nanoparticle as it attempts to depin itself.

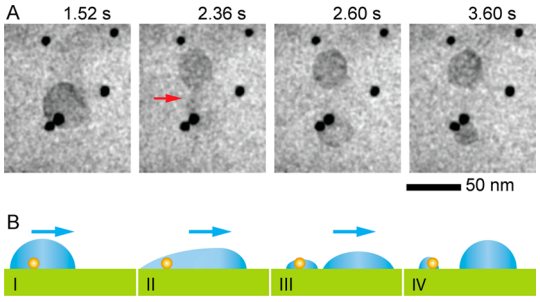

Figure 3. Droplet splitting during depinning. (A) Nanodroplet splitting during its depinning. Here, the nanodroplet forms a capillary bridge (red arrow) prior to splitting and leaving behind a smaller nanodroplet as it detaches from the gold nanoparticle, as schematically illustrated in (B).

of long wave hydrodynamics for the nanodroplet, a structural hump model to approximate the nanoparticle morphology, and interfacial disjoining pressure exerted by the substrate on the fluid film. Using the long wave approximation,[36] the thickness of a liquid film h evolves in two-dimensional space x, y, and time t according to

$$\partial_t h = -\nabla\cdot\left\{\frac{h^3}{3\mu}[\nabla(\gamma\nabla^2(h+S)+\Pi)+F_x]\right\} \quad (1)$$

where γ is the surface tension, μ is the dynamic viscosity, $S(x,y)$ is the surface topography including the nanoparticle, $\Pi(h)$ is the disjoining stress, and F_x is the driving force density (force per unit volume) in the direction of directional force, here taken as x.

The nanoparticle is geometrically approximated as a hump that resembles a nanoparticle attached to a flat surface (see Supporting Information and Figure S4A). The disjoining stress due to a solid−liquid interaction is modeled as a sum of short-ranged repulsive and long-ranged attractive forces per unit area, $\Pi(h,x) = \Pi_0[(h_s/h)^n - (h_s/h)^m]$, where Π_0 is a constant and (n,m) are positive exponents chosen as (4,3).[36,37] Here, the same form and exponents are assumed for the disjoining pressures for both the substrate and the nanoparticle.

The full evolution (eq 1) is initialized by first solving for the steady drop shape numerically in the absence of any lateral force, before time-marching under a constant lateral force. All numerical solutions are performed on a finite elements solver (Comsol v3.5a), and mesh independence is verified in each case to within 5% accuracy for all dependent variables.

Most of the independent model parameters are nonadjustable; that is, surface tension $\gamma \approx 0.07$ nN/nm and dynamic viscosity $\mu \approx 0.001$ Pa·s are fixed constants based on bulk values at room temperature, and a nanoparticle diameter of 10 nm is based on TEM observations (Figure 4), best fit using a hump model. We propose a disjoining pressure constant $\Pi_0 \approx 0.35$ nN/nm^2, which corresponds to a contact angle of ~45° (close to reported values of 42 ± 2°[38,39]) and compares reasonably to the Hamaker constant (silicon nitride−water) of 5×10^{-20} J.[40] Referring to the experimentally observed drop area (Figure 4), we simulate a nanodroplet with a volume of $\sim 2 \times 10^4$ nm^3 with a similar apparent area. We assume that this volume remains constant within our observation time scales. As a further check on the parameter sensitivity, we examined a range of droplet volumes and disjoining pressure constants and showed that these parameter choices are robust and reasonable (see Supporting Information and Figure S4B).

Although the driving force due to the imaging electron beam tends to flatten and drive the drop laterally in a stochastic fashion,[32] here, for the purpose of clarity, we limit ourselves to a constant lateral driving force applied in a fixed direction. To simulate nanodrop behavior during depinning, we apply the critical depinning force, defined here as the minimum force necessary to separate the nanodroplet from the nanoparticles, in a direction either parallel or orthogonal to the nanoparticle pair. Here, the critical depinning force is estimated by interpolating the lateral driving force F_x between pinned (stable) and depinned (unstable) with less than 2% error.

Figure 4 shows simulation snapshots taken at time points that correspond to experimental frames by

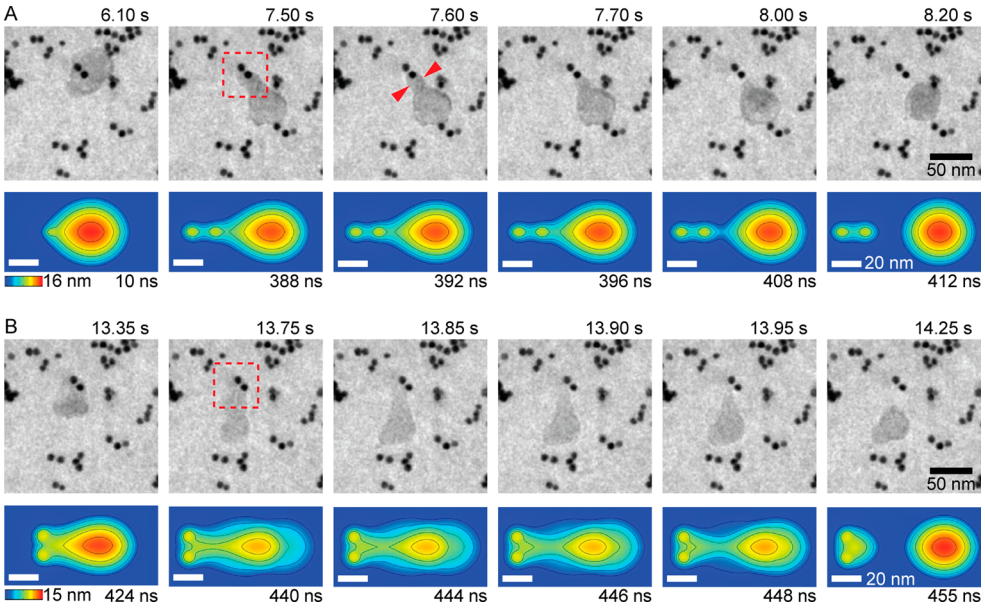

Figure 4. Depinning of the nanodroplet by 10 nm nanoparticles. (A,B) Two instances of the same nanodroplet depinning from the same nanoparticles reveal that pinning causes the stretch of the three-phase contact line. Simulation snapshots at indicated time points reveal comparable depinning behavior of the same nanodroplet that is critically driven in a direction either parallel (A) or orthogonal (B) to two model particles. Height difference from substrate (blue) to peak (red) is indicated below the first frames and equally partitioned to five elevation contours, as shown in each respective plot. Dashed boxes for frames at t = 7.50 s and t = 13.75 s highlight features of the capillary bridge (refer to text).

inspection. Driven parallel, we observe that the nanodroplet stretches in a globular shape, forms a liquid bridge, and detaches as a sliding drop, similar to that of a capillary pinch-off of a classical pendant drop[41] (Figure 4A). Driven off-tangent, we observe that the nanodroplet elongates in a more sheet-like manner, forms a wider and longer liquid bridge, and detaches as a stretched drop (Figure 4B). These differences are further accentuated in the simulated drop driven in a direction fully orthogonal compared to the parallel. It is notable that these simulated features, while mostly qualitative, compare well frame by frame with experimental observations in both cases. Furthermore, an inspection of the depinning times suggests a ratio of 4 ns simulation time to 0.1 s real time: a dramatic slowdown that alludes to significant deviation in apparent viscosities, which is discussed later.

The simulation in Figure 4B predicts a small residual water droplet left attached to the nanoparticles after depinning, but it may not be visible in that particular imaging contrast as it would be for the comparatively smaller nanodroplet in Figure 3. In addition, we note the curved thin liquid interfacial film surrounding the nanoparticle leading to the capillary bridge (red dashed boxes in Figure 4: t = 7.5 s and t = 13.75 s). Under a classical description neglecting absorbed liquid film, the driven drop would make a sharp contact line at the particle interface (as would a pendant drop experiment), but here, our simulation captured the smoothly varying interface due to the underlying interfacial substrate interaction.

From a practical standpoint, the critical depinning force can equivalently be viewed as the maximum lateral force that could be applied by a nanodroplet on a nanoparticle. For the simulations shown in Figure 4, the critical depinning forces are 1.26 nN for parallel depinning and 1.88 nN for orthogonal depinning, which also means that the adhesion force holding the nanoparticle in place exceeds 1 nN. As a check for experimental consistency, a crude estimate of the opposing capillary forces can be obtained from the apparent width of the capillary bridge. Taking a semicircular arclength of $l \sim \pi w/2$, where the bridge width is $w \sim 15$ nm by inspection (red arrows in Figure 4A: t = 7.6 s), we estimate the capillary force to be $\gamma l \sim 1.65$ nN, which compares reasonably with the magnitudes of the depinning forces obtained from simulations.

Separately, we find that the same nanodroplet depins from a single 10 nm particle at a critical force of 1.22 nN. This is similar to that of nanodroplet driven parallel to the nanoparticle pair (1.26 nN) and suggests that the bulk of the driving force is borne by just one nanoparticle, specifically the leading particle at the contact line. This is consistent with the drop dynamics observed in Figure 4A. For orthogonal depinning, the maximum force distributed evenly (assuming perfect symmetry) to each of the nanoparticles is 0.94 nN (1.88 nN total pinning force), which is consistently smaller than that for the case of either the single particle or parallel particle pair. From this, one infers that the forces per nanoparticle experienced by a cohort of three or more closely spaced nanoparticles are diminished, which corroborates the intuitive notion that tight clusters of nanoparticles or surface contaminants are more difficult to remove than isolated ones.

It is noteworthy that even at the limits of classical description, our model found general agreement in terms of simulated depinning forces and observed capillary forces, thus demonstrating that the observed nanodroplet depinning phenomenon can be adequately described by hydrodynamics, accounting for capillarity and interfacial stress. Due to the stochastic nature of the actual driving force, we have not conducted a rigorous analysis on the depinning time scales. However, given a capillary time scale $T \sim \mu(L/\gamma)$, where μ is the viscosity, L is the length scale, and γ is the surface tension, we see that the apparent viscosity of interfacial water scales directly with the apparent time scale $(\mu_{app}/\mu) \sim (T_{app}/T)$. For a given temporal ratio of roughly 0.1 s real time to 4 ns simulation time (Figure 4), the apparent viscosity of interfacial water is ~25 kPa·s, roughly 7 orders of magnitude greater than that of bulk water at room temperatures. Using apparent viscosity as the input, the model produces plots identical to those shown in Figure 4, except with respective time points rescaled by the viscosity ratio. In the case of our nanodroplets, which are effectively ~10 nm thick liquid films, this discrepancy, while significant, is consistent with apparent viscosities of interfacial or confined water reported in the literature,[42−44] although the exact nature of this phenomenon remains an open question.

CONCLUSION

We have outlined the dynamical behavior of water nanodroplets interacting with fixed nanoparticles on a substrate and provided a qualitative estimate for the depining forces, based on the stretching of the droplet prior to its detachment from nanoparticles. Under electron imaging, the nanodroplet stretches first, forming a short capillary bridge, followed by pinch-off, leaving behind a smaller residual nanodroplet attached to the nanoparticle. We find that the adhesion force[45] that holds a 10 nm gold particle at a fixed point on the SiN_x surface is greater than ~1 nN, the force needed to depin the nanodroplet. Due to the rapid miniaturizing of nanoscale devices, this has important implications on the activity of water nanocondensates and hydrodynamic limits to forces that could be applied on nanostructures or for removal of nanocontaminants. Future work can include nano-objects with different hydrophilic properties or shapes or nanopillars of different heights with well-characterized bending stiffness to probe for hydrodynamic forces at the nanoscale.

METHODS

Sample Preparation. Water containing 10 and 20 nm gold nanoparticles had a concentration of ~7×10^{11} and ~7×10^{10} particles/mL, respectively. We used ~1:8 to 1:10 dilution of aqueous 10 nm (Cat#GP01-10-20; Nanocs Inc. New York, NY, USA) and 20 nm (Cat#EM.GC20; TedPella Inc., Redding, CA, USA) nanoparticles in pure water (Cat#30072, Sigma-Aldrich Co., St Louis, MO, USA). A liquid cell was filled with ~400 nL of the postdiluted suspension using a syringe with fine tubing to prevent spill and membrane contamination. Next, the loading pockets of the liquid cell were sealed with a copper gasket. The sealed liquid cell was then loaded into a customized TEM holder and inserted into the TEM for imaging.

Liquid Cell Fabrication. The fabrication process of liquid cells is similar to that described by Zheng *et al.*[26] Our liquid cells were assembled from two ~3×3 mm^2 Si chips (top chip and bottom chip), each with a ~20 nm thick SiN_x membrane window with dimensions of ~20×50 μm^2 at the center of the chip. In addition, the top chip contains two pockets for loading the nanoparticle suspension, and the bottom chip has a ~100 nm thick gold spacer to provide separation between the two membranes. The chips were fabricated from 200 μm thick double-side polished 4 in. (100) Si wafers with SiN_x film deposited on both sides by low-pressure chemical vapor deposition. The central windows, pockets, and grooves for separating individual chips are patterned on the SiN_x layer by photolithography, followed by deep reactive ion etching of the SiN_x layer. Next, KOH etching of the exposed Si creates the windows, pockets, and the grooves. For the bottom chip, a ~100 nm gold layer and a ~5 nm titanium adhesive coating were patterned on the membrane side using thermal evaporation and a lift-off process. Then, the chips were cleaved from the wafer along the grooves. Finally, the top chip and bottom chips were aligned based on the best overlap of the respective central windows and glued together to form a single liquid cell assembly.

Imaging and Image Processing. An FEI Tecnai T12 TEM, operated at an accelerating voltage of 120 kV with a LaB6 filament, was used for *in situ* imaging with electron fluxes ranging from 100 to 300 e/(Å^2·s). Movies were acquired at a rate of 20−25 frames per second with an ORIUS SC200 (Gatan, Inc.) CCD camera using 4×4 binning (512×512 pixels). Segmentation of movie frames was implemented in the Miniconda Python[46,47] distribution with built-in packages[48−52] to define both droplets and nanoparticles in the image series. A threshold-based algorithm was used to segment out the highly contrasted gold nanoparticles from the images. As a rule, any pixel that falls below a 5% threshold in intensity (dark regions) is assumed to be part of the gold nanoparticles and is therefore marked as "1" or "0" otherwise. To further reduce incorrect identification, connected pixels were also subjected to an area filter. The above procedures generate a binary image, where the gold nanoparticles are represented by specific regions recorded as "1". A 3D binary volume stack (where z coordinate represents time) was then assembled from the segmented image sequence, and the identified objects were labeled across different time points based on their (i) area (if the change in nanoparticle area between two consecutive frames was less than 10%, they were treated as the same object) and (ii) centroid position (if the change in nanoparticle centroid between two consecutive frames is less than 10 pixels, they were also treated as the same object).

The contrast of water nanodroplets is significantly poorer than those of gold nanoparticles. Therefore, we inverted raw images so that the droplet appears brighter than the background and hence appears more distinctive. Next, we apply a Gaussian filter (σ = 2 pixel) before subtracting the background using a top-hat transform with a disk with a radius of 40 pixels as the structuring element. The resulting image is further refined using a Gaussian filter (σ = 2 pixels). Afterward, we use the Centroidal Voronoi tessellation algorithm[53] to divide the image into three clusters: (i) gold nanoparticles, (ii) nanodroplet, and (iii) background. The image was binarized by marking any pixel belonging to the nanodroplet cluster as "1" and "0" otherwise. Segmentation and labeling were further refined using the same method described in the preceding paragraph. The labeled

volume stack was used to evaluate the centroid position, area, and perimeter of the imaged nanodroplets. Lastly, those frames for which the clustering algorithm did not work were segmented manually.

Conflict of Interest: The authors declare no competing financial interest.

Acknowledgment. We thank Howard A. Stone for his helpful comments and suggestions. This work is supported in part by the Singapore National Research Foundation under CRP Award No. NRF-CRP9-2011-04.

Supporting Information Available: The Supporting Information is available free of charge on the ACS Publications website at DOI: 10.1021/acsnano.5b03078.

Additional experimental details and figures (PDF)
Video 1 (AVI)
Video 2 (AVI)

REFERENCES AND NOTES

1. Quéré, D. Wetting and roughness. *Annu. Rev. Mater. Res.* **2008**, *38*, 71–99.
2. Savva, N.; Pavliotis, G. A.; Kalliadasis, S. Contact Lines Over Random Topographical Substrates. Part 2. Dynamics. *J. Fluid Mech.* **2011**, *672*, 384–410.
3. de Gennes, P. G. Wetting: Statics and Dynamics. *Rev. Mod. Phys.* **1985**, *57*, 827–863.
4. Deegan, R. D.; Bakajin, O.; Dupont, T. F.; Huber, G.; Nagel, S. R.; Witten, T. A. Capillary Flow as the Cause of Ring Stains from Dried Liquid Drops. *Nature* **1997**, *389*, 827–829.
5. Weon, B. M.; Je, J. H. Self-Pinning by Colloids Confined at a Contact Line. *Phys. Rev. Lett.* **2013**, *110*, 028303.
6. Nguyen, T. A. H.; Hampton, M. A.; Nguyen, A. V. Evaporation of Nanoparticle Droplets on Smooth Hydrophobic Surfaces: the Inner Coffee Ring Deposits. *J. Phys. Chem. C* **2013**, *117*, 4707–4716.
7. Bonn, D.; Eggers, J.; Indekeu, J.; Meunier, J.; Rolley, E. Wetting and Spreading. *Rev. Mod. Phys.* **2009**, *81*, 739–805.
8. Herminghaus, S.; Brinkmann, M.; Seemann, R. Wetting and Dewetting of Complex Surface Geometries. *Annu. Rev. Mater. Res.* **2008**, *38*, 101–121.
9. Nosonovsky, M.; Bhushan, B. Superhydrophobic Surfaces and Emerging Applications: Non-Adhesion, Energy, Green Engineering. *Curr. Opin. Colloid Interface Sci.* **2009**, *14*, 270–280.
10. Dong, H.; Cheng, M.; Zhang, Y.; Wei, H.; Shi, F. Extraordinary Drag-reducing Effect of a Superhydrophobic Coating on a Macroscopic Model Ship at High Speed. *J. Mater. Chem. A* **2013**, *1*, 5886–5891.
11. Zhang, S.; Ouyang, X.; Li, J.; Gao, S.; Han, S.; Liu, L.; Wei, H. Underwater Drag-Reducing Effect of Superhydrophobic Submarine Model. *Langmuir* **2015**, *31*, 587–593.
12. Nishimoto, S.; Bhushan, B. Bioinspired Self-Cleaning Surfaces with Superhydrophobicity, Superoleophobicity and Superhydrophilicity. *RSC Adv.* **2013**, *3*, 671–690.
13. Wisdom, K. M.; Watson, J. A.; Qu, X.; Liu, F.; Watson, G. S.; Chen, C.-H. Self-Cleaning of Superhydrophobic Surfaces by Self-Propelled Jumping Condensate. *Proc. Natl. Acad. Sci. U. S. A.* **2013**, *110*, 7992–7997.
14. Epstein, A. K.; Wong, T.-S.; Belisle, R. A.; Boggs, E. M.; Aizenberg, J. Liquid-Infused Structured Surfaces with Exceptional Anti-Biofouling Performance. *Proc. Natl. Acad. Sci. U. S. A.* **2012**, *109*, 13182–13187.
15. Hasan, J.; Crawford, R. J.; Ivanova, E. P. Antibacterial Surfaces: the Quest for a New Generation of Biomaterials. *Trends Biotechnol.* **2013**, *31*, 295–304.
16. Mattia, D.; Gogotsi, Y. Review: Static and Dynamic Behavior of Liquids Inside Carbon Nanotubes. *Microfluid. Nanofluid.* **2008**, *5*, 289–305.
17. Naguib, N.; Ye, H.; Gogotsi, Y.; Yazicioglu, A. G.; Megaridis, C. M.; Yoshimura, M. Observation of Water Confined in Nanometer Channels of Closed Carbon Nanotubes. *Nano Lett.* **2004**, *4*, 2237–2243.
18. Varanasi, K. K.; Hsu, M.; Bhate, N.; Yang, W.; Deng, T. Spatial Control in the Heterogeneous Nucleation of Water. *Appl. Phys. Lett.* **2009**, *95*, 094101.
19. Dietz, C.; Rykaczewski, K.; Fedorov, A. G.; Joshi, Y. Visualization of Droplet Departure on a Superhydrophobic Surface and Implications to Heat Transfer Enhancement during Dropwise Condensation. *Appl. Phys. Lett.* **2010**, *97*, 033104.
20. Hong, S. J.; Chang, C. C.; Chou, T. H.; Sheng, Y. J.; Tsao, H. K. A Drop Pinned by a Designed Patch on a Tilted Superhydrophobic Surface: Mimicking Desert Beetle. *J. Phys. Chem. C* **2012**, *116*, 26487–26495.
21. Wu, J.; Xia, J.; Lei, W.; Wang, B. Advanced Understanding of Stickiness on Superhydrophobic Surfaces. *Sci. Rep.* **2013**, *3*, 3268.
22. Thiele, U.; Knobloch, E. On the Depinning of Driven Drop on a Heterogeneous Substrate. *New J. Phys.* **2006**, *8*, 313.
23. Asgari, M.; Moosavi, A. Interaction of 3D Dewetting Nanodroplets on Homogeneous and Chemically Heterogeneous substrates. *J. Phys.: Condens. Matter* **2014**, *26*, 225001.
24. Vahid, A.; Moosavi, A. Morphology of Nanodroplets on Structured Surfaces. *J. Phys. D: Appl. Phys.* **2013**, *46*, 215302.
25. Williamson, M. J.; Tromp, R. M.; Vereecken, P. M.; Hull, R.; Ross, F. M. Dynamic Microscopy of Nanoscale Cluster Growth at the Solid-Liquid Interface. *Nat. Mater.* **2003**, *2*, 532–536.
26. Zheng, H.; Smith, R. K.; Jun, Y.; Kisielowski, C.; Dahmen, U.; Alivisatos, A. P. Observation of Single Colloidal Platinum Nanocrystal Growth Trajectories. *Science* **2009**, *324*, 1309–1312.
27. Barkay, Z. Dynamic Study of Nanodroplet Nucleation and Growth on Self-Supported Nanothick Liquid Films. *Langmuir* **2010**, *26*, 18581–18584.
28. Barkay, Z. *In Situ* Imaging of Nano-Droplet Condensation and Coalescence on Thin Water Films. *Microsc. Microanal.* **2014**, *20*, 317–322.
29. Huang, T. W.; Liu, S. Y.; Chuang, Y. J.; Hsieh, H. Y.; Tsai, C. Y.; Wu, W. J.; Tsai, C. T.; Chang, C. S.; Mirsaidov, U. M.; Matsudaira, P.; et al. Dynamics of Hydrogen Nanobubbles in KLH Protein Solution Studied with *In-Situ* Wet-TEM. *Soft Matter* **2013**, *9*, 8856–8861.
30. Grogan, J. M.; Schneider, N. M.; Ross, F. M.; Bau, H. H. Bubble and Pattern Formation in Liquid Induced by an Electron Beam. *Nano Lett.* **2014**, *14*, 359–364.
31. Mirsaidov, U. M.; Zheng, H.; Bhattacharya, D.; Casana, Y.; Matsudaira, P. Direct Observation of Stick-Slip Movements of Water Nanodroplets Induced by an Electron Beam. *Proc. Natl. Acad. Sci. U. S. A.* **2012**, *109*, 7187–7190.
32. Leong, F. Y.; Mirsaidov, U. M.; Matsudaira, P.; Mahadevan, L. Dynamics of a Nanodroplet under a Transmission Electron Microscope. *Phys. Fluids* **2014**, *26*, 012003.
33. Rossi, M. P.; Ye, H.; Gogotsi, Y.; Babu, S.; Ndungu, P.; Bradley, J.-C. Environmental Scanning Electron Microscopy Study of Water in Carbon Nanopipes. *Nano Lett.* **2004**, *4*, 989–993.
34. Gogotsi, Y.; Libera, J. A.; Güvenç-Yazicioglu, A.; Megaridis, C. M. *In Situ* Multiphase Fluid Experiments in Hydrothermal Carbon Nanotubes. *Appl. Phys. Lett.* **2001**, *79*, 1021–1023.
35. Abdelsalam, M. E.; Bartlett, P. N.; Kelf, T.; Baumberg, J. Wetting of Regularly Structured Gold Surfaces. *Langmuir* **2005**, *21*, 1753–1757.
36. Oron, A.; Davis, S. H.; Bankoff, S. G. Long-Scale Evolution of Thin Liquid Films. *Rev. Mod. Phys.* **1997**, *69*, 931–980.
37. Schwartz, L. W.; Eley, R. R. Simulation of Droplet Motion on Low-Energy and Heterogeneous Surfaces. *J. Colloid Interface Sci.* **1998**, *202*, 173–188.
38. Kaware, R.; Desai, S. Molecular Dynamics Modeling of Water Nanodroplet Spreading on Topographically Patterned Silicon Dioxide and Silicon Nitride Substrates. *IIE Transactions.* **2015**, *47*, 767–782.
39. Pignataro, B.; Grasso, G.; Renna, L.; Marletta, G. Adhesion Properties on Nanometric Scale of Silicon Oxide and Silicon Nitride Surfaces Modified by 1-Octadecene. *Surf. Interface Anal.* **2002**, *33*, 54–58.
40. Bergström, L. Hamaker Constants of Inorganic Materials. *Adv. Colloid Interface Sci.* **1997**, *70*, 125–169.

41. Baroud, C. N.; Gallaire, F.; Dangla, R. Dynamics of Microfluidic Droplets. *Lab Chip* **2010**, *10*, 2032–2045.
42. Ortiz-Young, D.; Chiu, H.-C.; Kim, S.; Voïtchovsky, K.; Riedo, E. The Interplay between Apparent Viscosity and Wettability in Nanoconfined Water. *Nat. Commun.* **2013**, *4*, 2482.
43. Zhu, Y. X.; Granick, S. Viscosity of Interfacial Water. *Phys. Rev. Lett.* **2001**, *87*, 096104.
44. Major, R. C.; Houston, J. E.; McGrath, M. J.; Siepmann, J. I.; Zhu, X. Y. Viscous Water Meniscus under Nanoconfinement. *Phys. Rev. Lett.* **2006**, *96*, 177803.
45. de Gennes, P. G. Brownian Motion with Dry Friction. *J. Stat. Phys.* **2005**, *119*, 953–962.
46. Oliphant, T. E. Python for Scientific Computing. *Comput. Sci. Eng.* **2007**, *9*, 10–20.
47. Millman, K. J.; Aivazis, M. Python for Scientists and Engineers. *Comput. Sci. Eng.* **2011**, *13*, 9–12.
48. Bradski, G. The Open CV Library. *Dr. Dobb's Journal of Software Tools*, 2000; http://www.drdobbs.com/open-source/the-opencv-library/184404319.
49. Hunter, J. D. Matplotlib: A 2D Graphics Environment. *Comput. Sci. Eng.* **2007**, *9*, 90–95.
50. Behnel, S.; Bradshaw, R.; Citro, C.; Dalcin, L.; Seljebotn, D. S.; Smith, K. Cython: The Best of Both Worlds. *Comput. Sci. Eng.* **2011**, *13*, 31–39.
51. van der Walt, S.; Colbert, S. C.; Varoquaux, G. The NumPy Array: A Structure for Efficient Numerical Computation. *Comput. Sci. Eng.* **2011**, *13*, 22–30.
52. van der Walt, S.; Schonberger, J. L.; Nunez- Iglesias, J.; Boulogne, F.; Warner, J. D.; Yager, N.; Gouillart, E.; Yu, T. Scikit-Image: Image Processing in Python. *PeerJ* **2014**, *2*, e453.
53. Du, Q.; Gunzburger, M.; Ju, L.; Wang, X. Centroidal Voronoi Tessellation Algorithms for Image Compression, Segmentation, and Multichannel Restoration. *J. Math. Imaging Vis.* **2006**, *24*, 177–194.